J. Fluid Mech. (2011), *vol.* 678, *pp.* 511–534. © Cambridge University Press 2011
doi:10.1017/jfm.2011.123

Separated inviscid sheet flows

BUM-SANG YOON[1,2] AND YURIY A. SEMENOV[1]†

[1]School of Naval Architecture and Ocean Engineering University of Ulsan, 102 Daehakro, Ulsan 680-749, Republic of Korea

[2]WCU team, University of Ulsan, 102 Daehakro, Ulsan 680-749, Republic of Korea

(Received 11 March 2010; revised 27 February 2011; accepted 9 March 2011; first published online 3 May 2011)

A steady sheet flow of an inviscid incompressible fluid along a curvilinear surface ending with a rounded trailing edge is considered in the presence of gravity. The effect of surface tension is ignored. The formulation of the problem is applicable to the study of free-surface flows over obstacles in channels, weirs and spillways, and pouring flows. An advanced hodograph method is employed for solving the problem, which is reduced to a system of two integro-differential equations in the velocity modulus on the free surface and in the slope of the bottom surface. These equations are derived from the dynamic and kinematic boundary conditions. The Brillouin–Villat criterion is applied to determine the location of the point of flow separation from the rounded trailing edge. Results showing the effect of gravity on the flow detachment and the geometry of the free boundaries are presented over a wide range of Froude numbers including both subcritical and supercritical flows. For supercritical flows two families of solutions for an arbitrary bottom shape are reproduced. It is shown that the additional condition requiring the free surface to be flat at a finite distance from the end of the channel selects a unique solution for a given bottom height and geometry for supercritical flows. This solution is continuous in going from the subcritical to the supercritical flow regime.

Key words: channel flow, critical layers, solitary waves

1. Introduction

The nonlinear theory of two-dimensional sheet flows of an inviscid incompressible fluid includes several problems presented in the literature separately. They are channel flows with obstruction, pouring flows, flows over weirs and spillways, and flows around nozzles. In these problems, gravity plays an important role as a driving mechanism of motion.

Channel flows with obstruction were studied by Forbes & Schwartz (1982) and Vanden-Broeck (1987) for a semicircular obstacle and Dias & Vanden-Broeck (1989) for a triangular obstacle in a straight channel using the conformal mapping method coupled with the boundary integral method or the series truncation method (Dias & Vanden-Broeck 1989) to satisfy the dynamic boundary condition on the free surface. The application of the above methods to an arbitrarily shaped channel bottom requires a more sophisticated technique of conformal mapping transformation. By using the Cauchy integral equation formula, Dias & Vanden-Broeck (2004) derived a system of integral equations for channel flows with an arbitrarily shaped bottom, and they predicted a new type of flow called generalized hydraulic falls.

† Email address for correspondence: semenov@a-teleport.com

https://doi.org/10.1017/jfm.2011.123 Published online by Cambridge University Press

Pouring flows over a corner trailing edge and flows over thin and rectangular weirs were studied by Vanden-Broeck & Keller (1986, 1987, 1989), Dias, Vanden-Broeck & Keller (1988) and Dias & Tuck (1991). One of the interesting issues relating to pouring flows is the determination of the point of flow separation from the trailing edge of the channel, which is known as the 'teapot effect' studied by Reiner (1956) experimentally. The separation point may be located on the upper side of the nozzle at relatively high velocities or run over the edge reaching the underside of the nozzle at lower velocities. In the latter case the velocity of the sheet flow reverses direction and becomes opposite to the inflow velocity. Many authors have discussed the possible role of the physical properties of the fluid such as viscosity and surface tension as well as effects of water-to-nozzle adhesion and gravity, but the role of each factor is still not fully understood.

Keller (1957) provided a theoretical explanation for the abrupt change in the velocity direction near the trailing edge due to hydrodynamic forces pressing the liquid to the edge. His explanation is based on an analytical solution of the problem of sheet flow of an inviscid fluid around a thin sharp trailing edge without separation, gravity or surface tension effects. The role which gravity may play in sheet flows was studied by Vanden-Broeck & Keller (1986) and Dias & Vanden-Broeck (1990). Vanden-Broeck & Keller (1989) also obtained a solution for a corner trailing edge when the liquid runs along the underside of the nozzle and then separates, but the gravity effect was not included. They predicted the 'teapot effect' and found that the point of separation can be located anywhere on a straight underside, but on a concave underside its location is determined by the Brillouin–Vilat condition (Brillouin 1911; Villat 1914).

Using the same mathematical approach, Vanden-Broeck & Keller (1987) studied the problem of free-surface flow over a thin weir for both a finite and an infinite depth and predicted a discharge coefficient which is in agreement with experimental observations. Dias & Tuck (1991) studied flows over rectangular weirs of finite depth for both the subcritical and the supercritical flow regimes. They found two families of solutions similar to those obtained for open channel flows with obstructions (Vanden-Broeck 1987; Dias & Vanden-Broeck 1989).

In this paper we present a nonlinear solution for steady sheet flows of an inviscid incompressible fluid moving along an arbitrarily shaped curvilinear bottom surface ending with a rounded trailing edge in the presence of gravity. This formulation naturally corresponds to pouring flows and flows over weirs with an arbitrarily shaped trailing edge. However, taking into consideration a sufficiently long length of the flow region and specifying a uniform boundary condition far downstream, we obtain channel flows with obstructions in the same formulation of the problem. Special attention is given to the effect of gravity on the location of the flow separation. Attention is also given to critical and supercritical pouring flows and to the formulation of an additional condition selecting a unique solution of the problem matchable with subcritical weir flows.

Our solution method follows that proposed by Joukovskii (1890) and extended by Chaplygin (1910) for steady jet flows of an ideal fluid, and it consists of deriving an expression for the flow potential. The key point of the method is the analytical construction of two governing functions: the complex velocity and the derivative of the complex potential defined in an auxiliary parameter region which satisfy the boundary conditions of the problem. A new methodology for constructing the complex velocity function has been presented in Semenov (2003) and Semenov & Yoon (2009). By using this approach, all one has to do is to specify boundary conditions for the complex

https://doi.org/10.1017/jfm.2011.123 Published online by Cambridge University Press

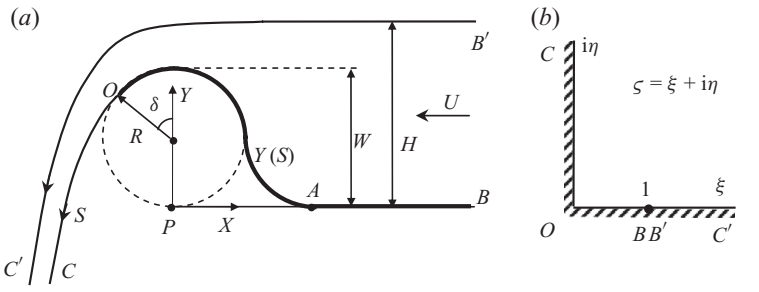


FIGURE 1. Sketch of the sheet flow (*a*) and the parameter plane (*b*).

velocity function, which are easy to obtain from the kinematic and dynamic boundary conditions of the problem, and then apply an integral formula ((2.7) in this paper) in order to obtain an expression for the required complex velocity function. The second expression, i.e. that for the derivative of the complex potential for channel flows is well known and can be obtained using Joukovskii's conformal mapping method (Joukovskii 1890) or Chaplygin's singularity method (Chaplygin 1910), both described in Gurevich (1965).

The problem is formulated in § 2, where an expression for the complex velocity is derived in integral form including the variation of the velocity modulus along the lower contour of the free surface and the variation of the velocity angle along the bottom of the channel and upper contour of the free surface. This function is given in terms of an auxiliary parameter variable, ς, which lies in the first quadrant corresponding to the physical flow domain. For a given bottom shape, we derive a system of integro-differential equations in the slopes of the channel bottom and upper free surface and in the velocity modulus along the lower free surface, both being functions of the parameter variable. These integral equations must be solved numerically to complete the solution of the problem. In § 3, a method of successive approximations adopted for solving the integral equations is outlined.

As a validation step, in § 4 careful comparisons are made with the results of Dias & Vanden-Broeck (1989) for channel flows with a triangular obstruction and with the results of Vanden-Broeck & Keller (1987) for weir flows. The results for pouring flows are reported in terms of the free surface and the angle of flow separation from a rounded trailing edge in a wide range of Froude numbers including both the subcritical and supercritical flow regimes. Comparisons with the results of Dias & Tuck (1991) for rectangular weirs are also presented and discussed.

2. Theoretical formulation and analysis

We consider the steady, two-dimensional potential flow of an inviscid, incompressible fluid moving along a curvilinear bottom, *BO*, ending with a circular cylinder of radius R sketched in figure 1(*a*). At upstream infinity, the velocity is U and the depth of the channel is H. The fluid is subject to the downward acceleration of gravity g and the disturbance height of the bottom W, which can be located arbitrarily far upstream from the end of the channel. At point O the sheet flow separates from the bottom surface and falls down under gravity. We introduce Cartesian coordinates x and y so that the shape of the bottom is determined by the functions $Y(S)$ and $X(S)$, where S is the spatial coordinate along the bottom.

https://doi.org/10.1017/jfm.2011.123 Published online by Cambridge University Press

Following Vanden-Broeck & Keller (1987), we introduce $L=(Q^2/g)^{1/3}$ as the unit length and $V=(Qg)^{1/3}$ as the unit velocity, where the discharge $Q=UH$. The dimensionless discharge $q=Q/VL=uh$ is equal to 1, where $u=U/V$ and $h=H/L$ are the dimensionless velocity and thickness of the liquid layer. By using these definitions we can express the Froude number

$$F=\frac{U}{\sqrt{gH}}=u^{3/2} \tag{2.1}$$

and the velocity magnitude on the free surface using the Bernoulli equation

$$v=u\sqrt{1+\frac{2(1-y/h)}{F^2}}, \tag{2.2}$$

assuming the pressure on the free surface to be constant.

Let the first quadrant of the ς-plane, where the complex variable is $\varsigma=\xi+\mathrm{i}\eta$, correspond to the flow region in the physical plane. Conformal mapping allows us to choose the location of three points O, C and B as shown in figure 1(b). Then the interval $0<\xi<1$ of the real axis corresponds to the bottom of the channel, the interval $1<\xi<\infty$ corresponds to the upper free surface $B'C'$, and the imaginary η-axis of the parameter region corresponds to the free surface OC. We introduce the complex potential $w=\varphi+\mathrm{i}\psi$, where φ is the flow potential and ψ is the stream function. The solution of the problem is sought in parametric form (Joukovskii 1890) by determining two functions, which are the complex conjugate velocity, $\mathrm{d}w/\mathrm{d}z$, and the derivative of the complex potential, $\mathrm{d}w/\mathrm{d}\varsigma$, both defined in the parameter region ς. Once expressions for these functions have been determined, the solution of the problem, i.e. the flow boundaries and the velocity field in the flow region, is determined as follows:

$$v_x-\mathrm{i}v_y=\frac{\mathrm{d}w}{\mathrm{d}z}(\varsigma),\quad z(\varsigma)=z(0)+\int_0^{\varsigma}\frac{\mathrm{d}w}{\mathrm{d}\varsigma'}\Big/\frac{\mathrm{d}w}{\mathrm{d}z}\,\mathrm{d}\varsigma'. \tag{2.3}$$

Here, $z(\varsigma)$ is a point in the flow region and v_x and v_y are the x- and y-components of the velocity at this point.

2.1. *Governing expressions*

In order to determine the derivative of the complex potential, $\mathrm{d}w/\mathrm{d}\varsigma$, we note that the region of the complex potential corresponding to the flow region in the physical plane is the infinite strip $-\infty<\varphi<\infty$ of width $\psi_{B'C'}-\psi_{BC}=q$ since $q=Q/(UH)$ is the dimensionless flow rate across the channel. At point O ($\varsigma=0$), the mapping of the first quadrant onto the w-plane is not conformal because the corner point of the angle of $\pi/2$ in the ς-plane corresponds to the same point in the w-plane with an angle equal to π. Thus, the local behaviour of the function $w(\varsigma)$ in the vicinity of $\varsigma=0$ is $w\sim\varsigma^2$ and $\mathrm{d}w/\mathrm{d}\varsigma\sim\varsigma$. At point C ($\varsigma=1$), there is a source of strength q, to which a logarithmic singularity corresponds, i.e. $w\sim\ln(\varsigma-1)$ and thus $\mathrm{d}w/\varsigma\sim(\varsigma-1)^{-1}$. By extending the first quadrant onto the whole complex plane ς and using the symmetry principle, we should add the same type of singularity at the point $\varsigma=-1$ symmetric to the point $\varsigma=1$ about the imaginary axis to provide a constant value of the function $\psi=\mathrm{Im}(w)$ on both the real and imaginary axes of the first quadrant in the ς-plane. Because there are no other singularities in the function $w(\varsigma)$, by using the Liouville theorem we can determine the complex potential function and its derivative as follows:

$$\frac{\mathrm{d}w}{\mathrm{d}\varsigma}=\frac{2q}{\pi}\frac{\varsigma}{\varsigma^2-1},\quad w=\frac{q}{\pi}\ln(1-\varsigma^2). \tag{2.4}$$

https://doi.org/10.1017/jfm.2011.123 Published online by Cambridge University Press

The range of values of the complex velocity function corresponding to the first quadrant is unknown *a priori*; therefore, an explicit conformal transformation of the first quadrant onto the complex velocity plane is a difficult problem. At this stage we assume that the magnitude of the velocity, v, and its argument, $\gamma = -\beta_i$, $i = 1, 2$, where β_1 is the slope of the bottom surface and β_2 is the slope of the upper free surface $B'C'$, are known as functions of the parameter variables η and ξ, respectively. Using the above definitions, the boundary conditions for the complex velocity function $\mathrm{d}w/\mathrm{d}z$ can be written as follows:

$$\arg\left(\frac{\mathrm{d}w}{\mathrm{d}z}\right) = \gamma(\xi) = \begin{cases} -\beta_1(\xi), & 0 < \xi < 1, \quad \eta = 0, \\ -\beta_2(\xi), & 1 < \xi < \infty, \quad \eta = 0, \end{cases} \tag{2.5}$$

$$\left|\frac{\mathrm{d}w}{\mathrm{d}z}\right| = v(\eta), \quad 0 < \eta < \infty, \quad \xi = 0. \tag{2.6}$$

The problem is then to find the function $\mathrm{d}w/\mathrm{d}z$ in the first quadrant of the parameter plane which satisfies the boundary conditions (2.5) and (2.6). The formula (Semenov 2003; Semenov & Yoon 2009)

$$\frac{\mathrm{d}w}{\mathrm{d}z} = v(\infty)\exp\left[\frac{1}{\pi}\int_0^\infty \frac{\mathrm{d}\gamma}{\mathrm{d}\xi}\ln\left(\frac{\varsigma+\xi'}{\varsigma-\xi'}\right)\mathrm{d}\xi' - \frac{\mathrm{i}}{\pi}\int_0^\infty \frac{\mathrm{d}\ln v}{\mathrm{d}\eta'}\ln\left(\frac{\varsigma-\mathrm{i}\eta'}{\varsigma+\mathrm{i}\eta'}\right)\mathrm{d}\eta' + \mathrm{i}\gamma(\infty)\right] \tag{2.7}$$

gives the solution of the mixed boundary-value problem (2.5) and (2.6). It can be easily verified that for $\varsigma = \xi$ the argument of the function $\mathrm{d}w/\mathrm{d}z$ is the function $\gamma(\xi)$, while for $\varsigma = \mathrm{i}\eta$ the magnitude of $\mathrm{d}w/\mathrm{d}z$ is the function $v(\eta)$, i.e. the boundary conditions (2.5) and (2.6) are satisfied.

Taking into account that $\gamma = -\beta_i$, $\arg(\varsigma - \xi') = \arg(\xi' - \varsigma) + \mathrm{i}\pi$ and $\arg(\varsigma - \mathrm{i}\eta) = \arg(\mathrm{i}\eta - \varsigma) - \mathrm{i}\pi$, expression (2.5) can be rewritten as follows:

$$\frac{\mathrm{d}w}{\mathrm{d}z} = v_0\exp\left[\left\{\int_0^1 \frac{\mathrm{d}\beta_1}{\mathrm{d}\xi} + \int_1^\infty \frac{\mathrm{d}\beta_2}{\mathrm{d}\xi}\right\}\frac{1}{\pi}\ln\left(\frac{\xi'-\varsigma}{\xi'+\varsigma}\right)\mathrm{d}\xi' - \frac{\mathrm{i}}{\pi}\int_0^\infty \frac{\mathrm{d}\ln v}{\mathrm{d}\eta'}\ln\left(\frac{\mathrm{i}\eta'-\varsigma}{\mathrm{i}\eta'+\varsigma}\right)\mathrm{d}\eta' - \mathrm{i}\beta_0\right], \tag{2.8}$$

where $v_0 = v(0)$ and $\beta_0 = \beta(0) = \pi + \delta$ are the velocity magnitude and angle at point O. Here, it is also implied that the principal value of the function $\arg(\varsigma)$ is defined in the range $[-\pi, \pi]$.

The formulation of the problem in the ς-plane imposes a limitation on the prediction of the flow parameters far upstream and downstream from point O due to the logarithmic singularities in expression (2.4) for the complex potential at points $BB'(\varsigma = 1)$ and $CC'(\varsigma = \infty)$ and to the limited number of figures in the number representation when using standard 64-bit arithmetic tools. In order to overcome this limitation, we consider the flow potential φ and the stream function ψ as independent variables and determine the variables ξ and η from equation (2.4):

$$\left.\begin{aligned} \varsigma(w) &= [1 - \exp(w\pi/q)]^{1/2}, \quad w = \varphi + \mathrm{i}\psi, \quad -\infty < \varphi < \infty, \quad 0 \leqslant \psi \leqslant q, \\ \eta(\varphi) &= [\exp(\varphi\pi/q) - 1]^{1/2}, \quad 0 \leqslant \varphi < \infty, \quad \psi = 0, \\ \xi_1(\varphi) &= [1 - \exp(\varphi\pi/q)]^{1/2}, \quad -\infty < \varphi \leqslant 0, \quad \psi = 0, \\ \xi_2(\varphi) &= [1 + \exp(\varphi\pi/q)]^{1/2}, \quad -\infty < \varphi < \infty, \quad \psi = q. \end{aligned}\right\} \tag{2.9}$$

https://doi.org/10.1017/jfm.2011.123 Published online by Cambridge University Press

By substituting (2.9) into (2.8) we obtain the complex velocity as a function of the complex potential w in the following form:

$$\frac{\mathrm{d}w}{\mathrm{d}z} = v_0 \exp\left[\frac{1}{\pi}\int_0^{-\infty} \frac{\mathrm{d}\beta_1}{\mathrm{d}\varphi'} K_1(\varphi', w)\,\mathrm{d}\varphi' + \frac{1}{\pi}\int_{-\infty}^{\infty} \frac{\mathrm{d}\beta_2}{\mathrm{d}\varphi'} K_2(\varphi', w)\,\mathrm{d}\varphi' - \frac{\mathrm{i}}{\pi}\int_0^{\infty} \frac{\mathrm{d}\ln v}{\mathrm{d}\varphi'} K_3(\varphi', w)\,\mathrm{d}\varphi' - \mathrm{i}\beta_0\right], \quad (2.10)$$

where

$$K_i(\varphi', w) = \ln\left[\frac{\xi_i(\varphi') - \varsigma(w)}{\xi_i(\varphi') + \varsigma(w)}\right], i = 1, 2, \quad K_3(\varphi', w) = \ln\left[\frac{\mathrm{i}\eta(\varphi') - \varsigma(w)}{\mathrm{i}\eta'(\varphi') + \varsigma(w)}\right]. \quad (2.11)$$

The functions $K_i(\varphi, w)$, $i = 1, 3$, can be evaluated directly for $|\varphi| < M$ and $|w| < M$, where M is a chosen large number such that $\mathrm{e}^M < 10^{10}$, and asymptotically in other cases.

The function inverse to the complex velocity function (2.10)

$$\frac{\mathrm{d}z}{\mathrm{d}w} = \frac{1}{v_0} \exp\left[-\frac{1}{\pi}\int_0^{-\infty} \frac{\mathrm{d}\beta_1}{\mathrm{d}\varphi'} K_1(\varphi', w)\,\mathrm{d}\varphi' - \frac{1}{\pi}\int_{-\infty}^{\infty} \frac{\mathrm{d}\beta_2}{\mathrm{d}\varphi'} K_2(\varphi', w)\,\mathrm{d}\varphi' + \frac{\mathrm{i}}{\pi}\int_0^{\infty} \frac{\mathrm{d}\ln v}{\mathrm{d}\varphi'} K_3(\varphi', w)\,\mathrm{d}\varphi' + \mathrm{i}\beta_0\right] \quad (2.12)$$

is the derivative of the function $z(w)$ conformally mapping the infinite strip in the w-plane onto the flow region in the z-plane. The integration of (2.12) along $0 < \varphi < \infty$, $\psi = 0$ in the w-plane gives the free surface OC, its integration along $-\infty < \varphi < 0$, $\psi = 0$ gives the bottom surface, and its integration along $-\infty < \varphi < \infty$, $\psi = q$ gives the upper free surface $B'C'$. However, the functions $\beta_i(\varphi)$ and $v(\varphi)$ are still unknown and will be determined later in the following from the boundary conditions.

The hydrodynamic force D acting on the obstacle in the x-direction is evaluated by integrating the pressure along the bottom surface. By choosing $\rho g H W$ as a reference quantity, where ρ is the density, from the Bernoulli equation we have

$$C_D = \frac{D}{\rho g H W} = \frac{H}{W}\int_0^{-\infty} p \sin\beta_1\,\mathrm{d}s = \frac{H}{W}\int_0^{-\infty} \left[1 - \frac{y}{h} + \frac{F^2}{2}(1 - v^2)\right] \frac{\sin\beta_1}{v}\,\mathrm{d}\varphi. \quad (2.13)$$

2.2. *Integro-differential equations in the functions $\beta_i(\varphi)$ and $v(\varphi)$*

We introduce the spatial coordinate $s = S/L$ along the free surface OC, $s = s_\eta(\varphi)$, and along the bottom surface and the upper free surface $B'C'$, $s = s_{\xi i}(\varphi)$, $i = 1, 2$, respectively, as follows:

$$s_\eta(\varphi) = -\int_0^{\varphi} \left|\frac{\mathrm{d}z}{\mathrm{d}w}\right|_{w=\varphi'} \mathrm{d}\varphi' = -\int_0^{\varphi} \frac{\mathrm{d}\varphi'}{v(\varphi')}, \quad 0 \leqslant \varphi < \infty, \quad (2.14)$$

$$s_{\xi i}(\varphi) = \int_0^{\varphi} \left|\frac{\mathrm{d}z}{\mathrm{d}w}\right|_{w=\varphi'+\psi} \mathrm{d}\varphi', \quad \begin{cases} -\infty \leqslant \varphi < 0, & \psi = 0, \quad i = 1, \\ -\infty \leqslant \varphi < \infty, & \psi = q, \quad i = 2. \end{cases} \quad (2.15)$$

https://doi.org/10.1017/jfm.2011.123 Published online by Cambridge University Press

Since the function $\beta_1(s)$ is given by the bottom surface, the function $\beta_1(\varphi)$, in view of (2.15), is determined from the following integro-differential equation:

$$\frac{\mathrm{d}\beta_1}{\mathrm{d}\varphi} = \frac{\mathrm{d}\beta_1}{\mathrm{d}s}\frac{\mathrm{d}s_{\xi 1}}{\mathrm{d}\varphi} = \frac{\mathrm{d}\beta_1}{\mathrm{d}s}\frac{1}{v_0}\exp\left\{-\frac{1}{\pi}\int_0^{-\infty}\frac{\mathrm{d}\beta_1}{\mathrm{d}\varphi'}\,|K_1(\varphi',\varphi)|\,\mathrm{d}\varphi' - \frac{1}{\pi}\int_{-\infty}^{\infty}\frac{\mathrm{d}\beta_2}{\mathrm{d}\varphi'}\,|K_2(\varphi',\varphi)|\,\mathrm{d}\varphi' - \frac{1}{\pi}\int_0^{\infty}\frac{\mathrm{d}\ln v}{\mathrm{d}\varphi'}\left[\pi - 2\tan^{-1}\left(\frac{\eta(\varphi')}{\xi(\varphi)}\right)\right]\mathrm{d}\varphi'\right\}, \quad -\infty < \varphi < 0. \tag{2.16}$$

The unknown function $\beta_2(\varphi)$, which is the slope of the free surface $B'C'$, is determined from the dynamic boundary condition on the free surface. Let the function $y_2(\varphi)$ be the ordinate of the free surface $B'C'$ and the function $v_2(\varphi)$ be the corresponding velocity magnitude determined from (2.2). By equating the modulus of the complex velocity (2.10) to the function $v_2(\varphi)$, on some algebraic manipulation we obtain the following integral equation in the function $\beta_2(\varphi)$:

$$\frac{1}{\pi}\int_{-\infty}^{\infty}\frac{\mathrm{d}\beta_2}{\mathrm{d}\varphi'}\,|K_2(\varphi',w)|\,\mathrm{d}\varphi' = \ln\left(\frac{v_2(\varphi)}{v_0}\right) - \frac{1}{\pi}\int_0^{-\infty}\frac{\mathrm{d}\beta_1}{\mathrm{d}\varphi'}\,|K_1(\varphi',w)|\,\mathrm{d}\varphi' - \frac{1}{\pi}\int_0^{\infty}\frac{\mathrm{d}\ln v}{\mathrm{d}\varphi'}\left[\pi - 2\tan^{-1}\left(\frac{\eta(\varphi')}{\xi(\varphi)}\right)\right]\mathrm{d}\varphi', \tag{2.17}$$

where $w = \varphi + \mathrm{i}q$, $-\infty < \varphi < \infty$,

$$v_2(\varphi) = u\sqrt{1 + \frac{2[1 - y_2(\varphi)/h]}{F^2}}, \tag{2.18}$$

$$y_2(\varphi) = h + \mathrm{Im}\left[\int_{-\infty}^{\varphi}\left(\frac{\mathrm{d}z}{\mathrm{d}w}\right)_{w=\varphi'+iq}\mathrm{d}\varphi'\right], \tag{2.19}$$

$$u = \left|\frac{\mathrm{d}w}{\mathrm{d}z}\right|_{w=-\infty}. \tag{2.20}$$

On the free surface OC the velocity magnitude is determined from the dynamic boundary condition (2.2), whose differentiation gives the following integro-differential equation in the function $\mathrm{d}(\ln v)/\mathrm{d}\varphi$:

$$F^2\frac{v^2 h}{u^2}\frac{\mathrm{d}\ln v}{\mathrm{d}\varphi} = -\frac{\mathrm{d}y}{\mathrm{d}\varphi}, \quad 0 < \varphi < \infty. \tag{2.21}$$

By substituting $w = \varphi$, $0 < \varphi < \infty$ into (2.12) and taking into account that $\mathrm{d}\varphi = v\mathrm{d}s$, we can express $\mathrm{d}y/\mathrm{d}\varphi$ in terms of the velocity modulus and argument:

$$\frac{\mathrm{d}y}{\mathrm{d}\varphi} = \mathrm{Im}\left(\frac{\mathrm{d}z}{\mathrm{d}w}\right)_{w=\varphi} = \mathrm{Im}\left(\frac{\mathrm{d}s_\eta}{\mathrm{d}\varphi}\mathrm{e}^{\mathrm{i}\theta}\right) = \frac{1}{v(\varphi)}\sin\theta, \tag{2.22}$$

where

$$\theta = \frac{2}{\pi}\int_0^{-\infty}\frac{\mathrm{d}\beta_1}{\mathrm{d}\varphi'}\tan^{-1}\left(\frac{\eta(\varphi)}{\xi_1(\varphi')}\right)\mathrm{d}\varphi' + \frac{2}{\pi}\int_{-\infty}^{\infty}\frac{\mathrm{d}\beta_2}{\mathrm{d}\varphi'}\tan^{-1}\left(\frac{\eta(\varphi)}{\xi_2(\varphi')}\right)\mathrm{d}\varphi' + \frac{1}{\pi}\int_0^{\infty}\frac{\mathrm{d}\ln v}{\mathrm{d}\varphi'}\,|K_3(\varphi',\varphi)|\,\mathrm{d}\varphi' + \beta_0. \tag{2.23}$$

https://doi.org/10.1017/jfm.2011.123 Published online by Cambridge University Press

By substituting (2.22) into (2.21) and taking into account that from (2.1) $F^2 = u^3$, we obtain the integro-differential equation in the function $\mathrm{d}(\ln v)/\mathrm{d}\varphi$:

$$v^3 \frac{\mathrm{d}\ln v}{\mathrm{d}\varphi} + \sin\left[\frac{1}{\pi}\int_0^\infty \frac{\mathrm{d}\ln v}{\mathrm{d}\varphi'}\,|K_3(\varphi',\varphi)|\,\mathrm{d}\varphi' + P(\varphi)\right] = 0, \tag{2.24}$$

where $0 < \varphi < \infty$,

$$v(\eta) = v_0 \exp\left(\int_0^\eta \frac{\mathrm{d}\ln v}{\mathrm{d}\eta'}\,\mathrm{d}\eta'\right), \quad v_0^2 = u^2\left[1 + \frac{2(1-y_0/h)}{F^2}\right], \tag{2.25}$$

$$P(\varphi) = \frac{2}{\pi}\int_0^{-\infty} \frac{\mathrm{d}\beta_1}{\mathrm{d}\varphi'} \tan^{-1}\left(\frac{\eta(\varphi)}{\xi_1(\varphi')}\right)\mathrm{d}\varphi' + \frac{2}{\pi}\int_{-\infty}^{\infty} \frac{\mathrm{d}\beta_2}{\mathrm{d}\varphi'} \tan^{-1}\left(\frac{\eta(\varphi)}{\xi_2(\varphi')}\right)\mathrm{d}\varphi' + \beta(0). \tag{2.26}$$

The functions $\beta_1(\varphi)$ and $\beta_2(\varphi)$ are determined by the integral equations (2.16) and (2.17) on the boundary of the complex potential region w, $-\infty < \varphi < 0$, $\psi = 0$ and $-\infty < \varphi < \infty$, $\psi = q$, which corresponds to the whole real axis of the parameter plane ς. The velocity modulus function $v(\varphi)$ is determined by the integral equation (2.24) on the rest of the complex potential region w, $0 < \varphi < \infty$, $\psi = 0$, which corresponds to the whole imaginary axis of the parameter plane ς.

Note that the system of integral equations (2.16), (2.17) and (2.24) is closed, and the Froude number is determined from (2.1) and (3.15). It will be shown later from a numerical investigation of this system of equations that for $F < 1$ it possesses a unique solution, in which the Froude number is determined by the height of the trailing edge and the geometry of the bottom. For $F > 1$ (2.1) and (3.15) may be satisfied for different heights of the trailing edge bounded by some maximal value depending on a given Froude number.

2.3. *Flow separation condition*

For channels with a sharp trailing edge, the flow separation point is fixed, and thus the function $\beta_1(s)$ is known. For a smoothly shaped trailing edge, the flow separation position, $s = 0$, is unknown and should be determined from an additional condition. In the model of an ideal fluid, this condition is well known as the Brillouin–Villat criterion (Brillouin 1911; Villat 1914; Birkhoff & Zarantonello 1957). The physical meaning of this criterion consists in the fact that at the point of flow separation the pressure on the bottom surface reaches its minimum value, which is the pressure on the free surface. This condition also provides equality between the curvature of the free surface and that of the trailing edge at the point of separation. In terms of the velocity modulus along the bottom surface, the Brillouin–Villat criterion takes the form

$$\lim_{s\to 0} \frac{\mathrm{d}\ln v}{\mathrm{d}s} = 0, \tag{2.27}$$

where s is the spatial coordinate approaching the point of flow separation along the bottom surface.

By using the relation

$$\frac{\mathrm{d}\ln v}{\mathrm{d}s} = \frac{\mathrm{d}\ln v/\mathrm{d}\xi}{\mathrm{d}s/\mathrm{d}\xi} \tag{2.28}$$

https://doi.org/10.1017/jfm.2011.123 Published online by Cambridge University Press

and differentiating the function $v(\xi) = |\mathrm{d}w/\mathrm{d}z|_{\varsigma=\xi}$ with consideration of (2.8), the condition (2.27) takes the form

$$-\int_0^1 \frac{\mathrm{d}\beta_1}{\mathrm{d}\xi'}\frac{\mathrm{d}\xi'}{\xi'} - \int_1^\infty \frac{\mathrm{d}\beta_2}{\mathrm{d}\xi'}\frac{\mathrm{d}\xi'}{\xi'} + \int_0^\infty \frac{\mathrm{d}\ln v}{\mathrm{d}\eta'}\frac{\mathrm{d}\eta'}{\eta'} = 0, \tag{2.29}$$

where the derivatives of the functions β_1, β_2 and $\ln v$ can be easily determined using (2.4):

$$\frac{\mathrm{d}\beta_i}{\mathrm{d}\xi} = \frac{\mathrm{d}\beta_i}{\mathrm{d}\varphi}\frac{\mathrm{d}\varphi}{\mathrm{d}\xi} = \frac{\mathrm{d}\beta_i}{\mathrm{d}\varphi}\frac{2q}{\pi}\frac{\xi}{\xi^2-1}, \quad \frac{\mathrm{d}\ln v}{\mathrm{d}\eta} = \frac{\mathrm{d}\ln v}{\mathrm{d}\varphi}\frac{\mathrm{d}\varphi}{\mathrm{d}\eta} = \frac{\mathrm{d}\ln v}{\mathrm{d}\varphi}\frac{2q}{\pi}\frac{\eta}{\eta^2+1}. \tag{2.30}$$

Equation (2.29) is an equation in the unknown position of the point of flow separation on the rounded spout, which affects the function $\beta_1(\xi) = \beta_1[s(\xi)]$. Besides, this equation written in the parameter plane ς shows that the shape of the bottom and free surfaces can affect the location of the flow separation only within a distance that can be estimated as $|S| < 5H$. This can be seen as follows. If we assume that both on the channel bottom and on the free surface the velocity magnitude $v \sim 1$, then $\varphi \sim s$. From (2.9) we can find, for example, that for $|\varphi| = 5$ the values of $\eta \approx \xi \approx 2600$ and the value of $1-\xi \approx 10^{-7}$ for $\varphi = -5$. For very large or very small values of ξ and η, the integrals in expression (2.8) can be evaluated analytically if $|\varsigma| \sim 1$; thus, the effect of the bottom shape disappears for $1-\xi < 10^{-7}$ and $\xi > 2600$ corresponding to a flow region $|S| > 5H$.

3. Numerical method

First, the system of equations (2.16), (2.17) and (2.24) is truncated upstream and downstream at the points $-\varphi^*$ and φ^*, and the flow in the regions corresponding to $|\varphi| > \varphi^*$ is assumed to be uniform. The error introduced by such a truncation will be discussed later in § 4. In discrete form, the solution is sought on two fixed sets of points $\varphi_j^{(1)}$, $j = 1, \ldots, 3N$, and $\varphi_j^{(2)}$, $j = 1, \ldots, N$. The first set of points $\varphi_j^{(1)}$ decreases in the range $j = 1, \ldots, N$ from $\varphi_1^{(1)} = 0$ to $\varphi_N^{(1)} = -\varphi^*$ and then increases in the range $j = N+1, \ldots, 3N$ from $\varphi_{N+1}^{(1)} = -\varphi^*$ to $\varphi_{3N}^{(1)} = \varphi^*$. Such a distribution of the points $\varphi_j^{(1)}$ corresponds to a monotonic distribution of the points ξ_j, $j = 1, \ldots, 3N$, along the whole real axis of the parameter plane from $\xi_1 = 0$ to $\xi_{3N} = \xi^* \gg 1$ in accordance with (2.9). The second set of points $\varphi_j^{(2)}$ is distributed monotonically from $\varphi_1^{(2)} = 0$ to $\varphi_N^{(2)} = \varphi^*$, $j = 1, \ldots, N$, to a monotonic distribution of the points η_j, $j = 1, \ldots, N$, along the imaginary axis of the parameter plane.

The integrals appearing in the system of equations are evaluated using the linear interpolation of the functions $\beta_i(\xi)$, $i = 1, 2$, and $\ln v(\eta)$ on the intervals (ξ_{j-1}, ξ_j) and (η_{j-1}, η_j), respectively. The integrals in (2.8) may be evaluated for $\varsigma = \xi$ as follows:

$$\frac{1}{\pi}\int_0^1 \frac{\mathrm{d}\beta_1}{\mathrm{d}\xi}\ln\left(\frac{\xi'-\xi}{\xi'+\xi}\right)\mathrm{d}\xi' + \frac{1}{\pi}\int_1^\infty \frac{\mathrm{d}\beta_2}{\mathrm{d}\xi}\ln\left(\frac{\xi'-\xi}{\xi'+\xi}\right)\mathrm{d}\xi' = \Delta\beta_j a_j(\xi), \quad j = 1, \ldots, 3N, \tag{3.1}$$

where

$$\Delta\beta_j = \begin{cases} \beta_1(\xi_j) - \beta_1(\xi_{j-1}), & j = 1, \ldots, N, \\ \beta_2(\xi_j) - \beta_2(\xi_{j-1}), & j = N+1, \ldots, 3N, \end{cases} \tag{3.2}$$

$$a_j(\xi) = \frac{1}{\pi\Delta\xi_j}\int_{\xi_{j-1}}^{\xi_j} \ln\left(\frac{\xi'-\xi}{\xi'+\xi}\right)\mathrm{d}\xi'. \tag{3.3}$$

https://doi.org/10.1017/jfm.2011.123 Published online by Cambridge University Press

The integral in the last equation can be easily evaluated, and the result is a non-singular expression for the functions $a_j(\xi)$. Moreover, combining the terms ξ_j and ξ as ξ_j/ξ or $(\xi_j-1)/(\xi-1)$ depending on the values of the corresponding potentials φ_j and φ in the resulting expression, it is possible to obtain asymptotic expressions for the functions $a_j(\xi)$ in the cases $|\varphi_j| > M$ or $|\varphi| > M$, for which ξ_j or ξ becomes too large or (ξ_j-1) or $(\xi-1)$ becomes too small for direct computations due to the exponents in (2.9).

Thus, the coefficients $a_{ij}=a_j(\xi_i)$ may be calculated throughout the range $i, j=1,\ldots,3N$ without the limitations on the length of the channel arising in the computations.

In a similar way we obtain the coefficients

$$\left.\begin{aligned} b_{ij} &= \frac{2}{\pi\Delta\xi_j}\int_{\xi_{j-1}}^{\xi_j}\tan\left(\frac{\eta_i}{\xi'}\right)\mathrm{d}\xi', \quad c_{ij} = \frac{1}{\pi\Delta\eta_j}\int_{\eta_{j-1}}^{\eta_j}\ln\left(\frac{\eta'-\eta_i}{\eta'+\eta_i}\right)\mathrm{d}\eta', \\ d_{ij} &= \frac{1}{\pi\Delta\eta_j}\int_{\eta_{j-1}}^{\eta_j}\left[\pi-2\tan\left(\frac{\eta'}{\xi_i}\right)\right]\mathrm{d}\eta'. \end{aligned}\right\} \tag{3.4}$$

The method of successive approximations is applied to solve the system of nonlinear integral equations derived in § 2.2. In each successive approximation of the function $\beta_2(\varphi)$ determining the shape of the free surface $B'C'$, the integral equations (2.16) and (2.24) are solved using inner iteration procedures. The $(k+1)$th inner iteration procedure for solving the integral equation (2.16) is organized as follows:

$$\Delta\beta_i^{(k+1)} = \beta_1\left(s_i^{(k+1)}\right) - \beta_1\left(s_{i-1}^{(k+1)}\right), \quad i=2,\ldots,N, \tag{3.5}$$

$$s_i^{(k+1)} = s_{i-1}^{(k+1)} + \frac{\Delta\varphi_i}{v^{(k)}(0)}\exp\left[-\sum_{j=1}^{N}a_{ij}\Delta\beta_j^{(k)} - \sum_{j=N+1}^{3N}a_{ij}\Delta\beta_j + \sum_{j=1}^{N}d_{ij}\Delta\ln v_j\right], \quad s_1=0, \tag{3.6}$$

where (3.6) is (2.15) in discreet form.

The determination of the velocity magnitude on the free surface OC is a second inner iteration procedure. Taking into account the fact that the flow in the free falling jet OCC' is always supercritical, we can expect the convergence of the simple iteration process based on (2.2) instead of solving the integral equation (2.24). The $(k+1)$th inner approximation of the velocity magnitude is

$$v_i^{(k+1)} = u^{(k)}\sqrt{1+2(1-y_i^{(k+1)}/h)/F^{2(k)}}, \quad \Delta\ln v_i^{(k+1)} = \left(\ln\frac{v_i}{v_{i-1}}\right)^{(k+1)}, \quad i=1,\ldots,N, \tag{3.7}$$

where $y_i^{(k+1)}$, in view of (2.22), is obtained as

$$y_i^{(k+1)} = y_{i-1}^{(k+1)} + \frac{\Delta\varphi_i}{v_{i-(1/2)}^{(k)}}\sin\left[\sum_{j=1}^{3N}\Delta\beta_j b_{ij} + \sum_{j=1}^{N}\Delta\ln v_j^{(k)}c_{ij} + \beta(0)\right]. \tag{3.8}$$

The successive approximation of the function $\beta_2(\varphi)$ is obtained from the solution of the integral equation (2.17) at the points $\bar{\varphi}_i=(\varphi_{i-1}+\varphi_i)/2$ at fixed values of the functions $\beta_1(\varphi)$ and $\ln v(\varphi)$, which corresponds to the matrix system

$$\sum_{j=N+2}^{3N}\bar{a}_{ij}\Delta\beta_j^{(k+1)} = \ln\frac{v_{2i}^{(k)}}{v(0)} - \sum_{j=1}^{N}\bar{a}_{ij}\Delta\beta_j - \sum_{j=1}^{N}\bar{d}_{ij}\Delta\ln v_j, \quad i=N+2,\ldots,3N, \tag{3.9}$$

https://doi.org/10.1017/jfm.2011.123 Published online by Cambridge University Press

where the coefficients $\bar{a}_{ij}$ are evaluated at the points $\bar{\varphi}_i$, and

$$\bar{v}_{2i}^{(k)} = u^{(k)}\sqrt{1+2(1-\bar{y}_i^{(k)}/h)/F^{2(k)}}, \quad \bar{y}_i^{(k)} = (y_{i-1}^{(k)} + y_i^{(k)})/2, \tag{3.10}$$

$$y_i^{(k)} = y_{i-1}^{(k)} + \sin\bar{\beta}_i^{(k)}(s_i^{(k)} - s_{i-1}^{(k)}), \tag{3.11}$$

the points $s_i^{(k)}$being determined using (2.14). The upstream velocity at infinity $u^{(k)}$ is determined from (2.12) at $\varphi = -\infty$, whose discreet form is

$$u^{(k)} = v^{(k)}(0)\exp\left[\sum_{j=1}^{N}\bar{a}_{Nj}\Delta\beta_j + \sum_{j=N+1}^{3N}\bar{a}_{Nj}\Delta\beta_j^{(k)} + \sum_{j=1}^{N}\bar{d}_{Nj}\Delta\ln v_j\right]. \tag{3.12}$$

For subcritical flows $F<1$ in the outer iteration procedure for solving the integral equation (3.9), a new approximation of the Froude number is obtained by using (2.1):

$$F^{(k+1)} = (u^{(k)})^{3/2}. \tag{3.13}$$

Besides, the restriction $\beta_2^{(k)}(\varphi) > 0$ was applied to provide a monotonic decrease of the y-coordinate of the free surface $B'C'$. This restriction is required to get the convergence of the iteration procedure in the case of subcritical flows.

For supercritical flows $F>1$ there are two families of solution, which will be discussed later in § 4.3. The equation

$$F - u^{3/2} = 0 \tag{3.14}$$

is always satisfied at infinity for a given Froude number in some range of trailing edge heights. However, applying this condition at a finite distance from the trailing edge makes it possible to select a unique solution for a given bottom height and geometry such that the perturbation due to the end of the channel decays upstream at the fastest rate. In this case the free surface becomes flat at a finite distance from the end of the channel:

$$u = \left|\frac{\mathrm{d}w}{\mathrm{d}z}\right|_{w=-\varphi^{**}}, \tag{3.15}$$

where $\varphi^* < \varphi^{**} < \infty$. Equation (3.14) was solved by Newton's method.

The iterative process begins with $\beta_1(\varphi) \equiv 0$, $\beta_2(\varphi) \equiv 0$ and $\ln v(\varphi) \equiv \ln u$. The number N of discreet points was chosen in the range 100–800 to check the mesh independence and accuracy of the results. When solving the integral equation (3.9) for both subcritical and supercritical flows, several hundreds of iterations were required for the outer iterations to converge, and this was obtained using the under-relaxation method.

4. Results and discussion

4.1. *Validation of the numerical approach. Channel flows*

The formulation of the problem allows us to consider channel flows with obstructions if we choose the location of the obstacle far upstream from the trailing edge O, which in this case may be considered as a point far downstream from the obstacle where the flow becomes uniform with the velocity at infinity downstream. For example, by setting the value of the potential at some point on the obstacle equal to $\varphi^* = -10q$, we can estimate the distance between this point and point O as $s^*/h \approx |\varphi^*|/(uh) = 10$ since $uh = q$. The ratio $s^*/h \approx 10$ is large enough to consider the flow near point O as a uniform flow with a velocity equal to the velocity at infinity downstream. Thus,

https://doi.org/10.1017/jfm.2011.123 Published online by Cambridge University Press

N	$F=1.522$ Perturbed soliton wave	$W/L=0.48$ Perturbed uniform inflow	$F=1.3$ Perturbed soliton wave	$W/L=0.25$ Perturbed uniform inflow
100	1.550	1.189	1.362	0.9998
200	1.573	1.185	1.369	0.9989
400	1.573	1.185	1.382	0.9987
800	1.573	1.185	1.382	0.9986

TABLE 1. Effect of the mesh on the maximum wave elevation y_{max} for both a perturbed soliton wave and a perturbed uniform flow.

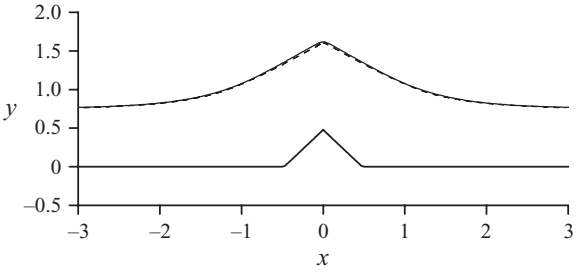


FIGURE 2. The limiting flow configuration of the soliton wave perturbed by a triangle at the bottom of the channel for Froude number $F=1.52$ and obstacle height $W/L=0.48$; the obtained results (solid line) are compared with the results of Dias & Vanden-Broeck (1989) shown by a dashed line.

we can set $\ln v(\varphi) \equiv \ln v_C$ on the free surface OC and solve only the two integro-differential equations (2.16) and (2.17). The velocity v_C may be equal to the inflow velocity u (the case where both the upstream and downstream flows are supercritical) or its conjugate value (Benjaminn 1966) if the flow regime changes from subcritical upstream to supercritical downstream.

For validation purposes we consider steady channel flows over a triangular obstacle at the bottom of the channel. Such a channel configuration has been studied in detail by Dias & Vanden-Broeck (1989), who used the series truncation method and presented various solutions of the problem. In figure 2, the free-surface profile obtained using the present method is shown and compared with the corresponding solution of Dias & Vanden-Broeck (1989) for triangle height $W/L=0.48$ and Froude number $F=1.52$. This solution is the limiting flow configuration corresponding to the perturbation of the soliton wave at which the velocity at the point of maximum elevation tends to zero and the angle between the free surfaces on the right and left sides tends to 120°. Note that the corner shape of the obstacle calls for an increase in the number of nodes φ_j corresponding to points s_j near the corner points of the obstacle. The shape of the triangle shown in figure 2 is the computed shape obtained by integration of expression (2.12).

To evaluate the accuracy and mesh independence of the results, several distributions with different numbers of nodes on the free and bottom surfaces were employed. Increasing the number of nodes on the bottom of the channel leads to a better agreement between the given and calculated shapes of the obstacle. 400 nodes on the bottom with a higher density of nodes near the corner points provide reasonably accurate computations of the bottom shape. This number of nodes was fixed to analyse the effect of the mesh on the free-surface shape. Table 1 gives the maximal

https://doi.org/10.1017/jfm.2011.123 Published online by Cambridge University Press

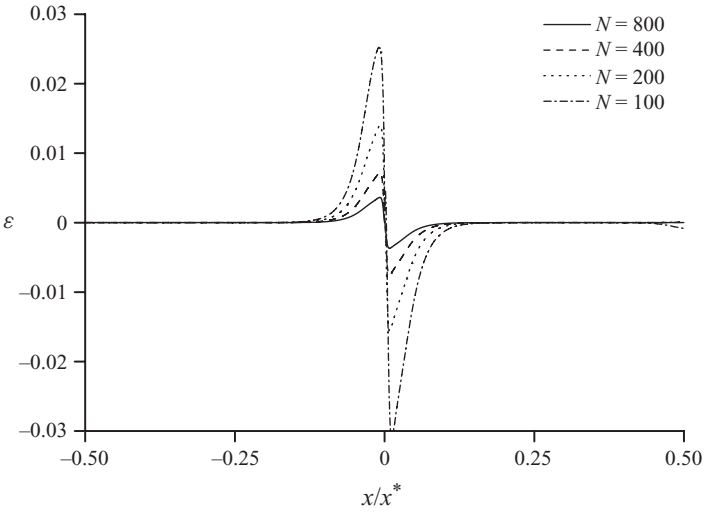


FIGURE 3. Effect of the mesh on the accuracy of the velocity magnitude along the free surface for the case shown in figure 2; the length taken in computations $X^* = 20H$.

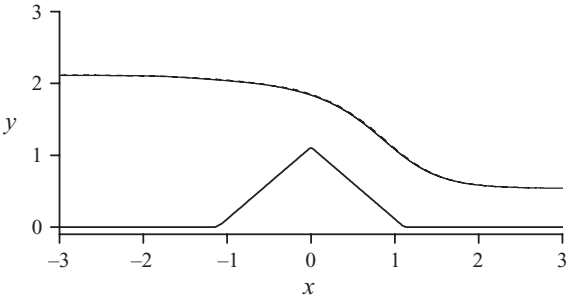


FIGURE 4. The free-surface profiles in a channel with a triangular obstacle of height $W/L = 1.103$ obtained by the present method (solid line) and the series truncation method (Dias & Vanden-Broeck 1989; dashed line). For both methods the computed Froude number $F = 0.32$.

height of the wave elevation predicted for two combinations of the Froude number and obstacle height. For the first case the Froude number $F = 1.522$ and the obstacle height $W/L = 0.48$, and for the second $F = 1.3$ and $W/L = 0.25$. Results are presented for both types of solution, namely a perturbed soliton wave and a perturbed uniform flow, which will be discussed later.

The effect of the mesh on the accuracy of the velocity magnitude along the free surface is shown in figure 3. The quantity

$$\varepsilon = v' - v \tag{4.1}$$

is the error in the computation of the velocity magnitude on the free surface. Here, $v' = |\mathrm{d}w/\mathrm{d}z|_{w=\varphi+iq}$ is the velocity magnitude provided by the expression for the complex velocity and v is the velocity magnitude obtained from the Bernoulli equation (2.18), in which the ordinate of the free surface is obtained by integrating expression (2.19). The convergence of the numerical method with increasing number of nodes is clearly seen. The free-surface profile corresponding to a subcritical upstream flow and a supercritical downstream flow is shown in figure 4. As can be seen, both obtained

https://doi.org/10.1017/jfm.2011.123 Published online by Cambridge University Press

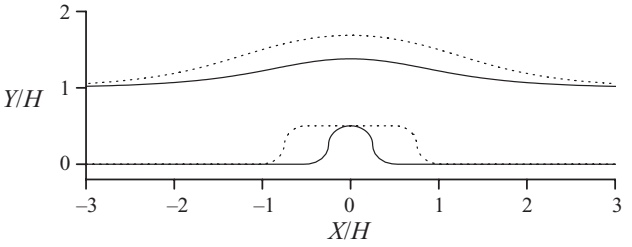


FIGURE 5. Effect of the obstacle width on the free-surface profile of the perturbed uniform flow for height $W/H = 0.5$ and Froude number $F = 1.6$. The width of the obstacle $B = 4R$ (solid line) and $B = 4R + H$ (dashed line) with $R = W/2$.

solutions in figures 2 and 4 (solid line) agree quite well with the solutions of Dias & Vanden-Broeck (1989) (dashed line). In addition to these comparisons, the other free-surface profiles corresponding to the cases presented in figures 1, 2(a) and 5 in the paper of Dias & Vanden-Broeck (1989) were computed with the same accuracy.

4.2. *Effect of the bottom shape on the free surface for channel flows*

The present formulation of the problem allows us to consider an arbitrary shape of the channel bottom, but we restrict our numerical analysis to obstacles consisting of circular arcs of radius R and straight lines if the width or height of the obstacle W exceeds $2R$. Then the slope of the bottom can be expressed as follows:

$$\beta_1(s) = \begin{cases} s/r, & 0 \leqslant |s| \leqslant \gamma r, \\ 2\gamma\,\mathrm{sgn}(s) - s/r, & \gamma r \leqslant |s| \leqslant 2\gamma r, \\ 0, & 2\gamma r \leqslant |s|\,, \end{cases} \tag{4.2}$$

where $r = R/H$ is the dimensionless radius of the circular arc, $\gamma = \cos^{-1}[1 - W/(2R)]$ for $W \leqslant 2R$ and the width of the obstacle $B \leqslant 4R\sin\gamma$. If $B > 4R\sin\gamma$, the start of the circular arc is shifted both to the right and to the left by the length $P = B/2 - 2R\sin\gamma$ relative to the point $s = 0$ ($x = 0$), which is the symmetry point of the obstacle as shown in figure 5.

The effect of the obstacle width on the free-surface profile is shown in figure 5 for the case of the uniform flow perturbed by an obstacle of height $W/H = 0.5$ and radius $R/W = 0.5$, which corresponds to arc angle $\gamma = \pi/2$. For the obstacle shown by a solid line the straight part is absent ($B = 4R = H$), while for that shown by a dashed line the length of the straight part $2P = H$ and the total width $B = 2H$. It can be seen that the increase in obstacle width results in about a twofold increase in the height of the wave.

Vanden-Broeck (1987) found that for supercritical flows there exists a range of Froude numbers $F^* < F < F^{**}$ in which the problem has two solutions for a given relative height of the semicircular obstacle $\alpha = W/H$. Here, F^* corresponds to the solution called a perturbation of a uniform flow, and F^{**} corresponds to the other called a perturbation of a soliton wave. In the study of Dias & Vanden-Broeck (1989) for the triangular shape of the obstacle a similar range of Froude numbers with two solutions was found too.

Figure 6 shows the relative maximum elevation

$$\tau = \frac{y_{max}}{h} - 1 \tag{4.3}$$

https://doi.org/10.1017/jfm.2011.123 Published online by Cambridge University Press

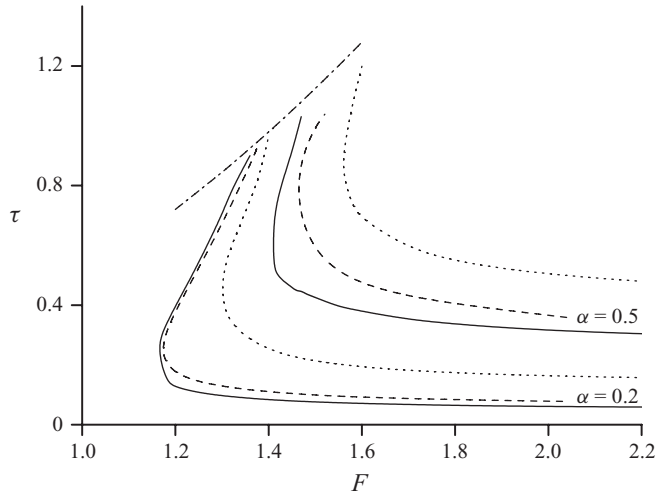


FIGURE 6. Effects of the obstacle shape and height α on the maximum elevation τ of the free surface versus Froude number: dashed lines correspond to the Vanden-Broeck (1987) results for a semicircular obstruction; solid/dotted lines correspond to the obstacles shown in figure 5 by solid/dotted lines, respectively; the dot-dashed line corresponds to the maximal wave elevation with a stagnation point on the free surface.

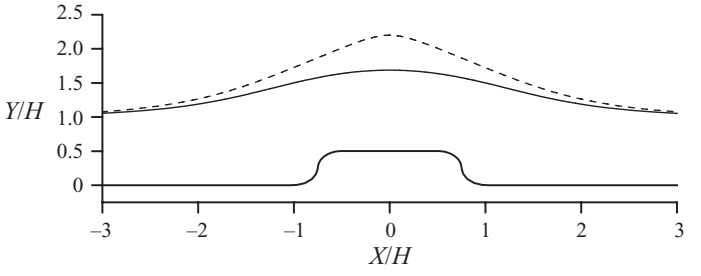


FIGURE 7. The free-surface profiles corresponding to the perturbed uniform flow (solid line) and the perturbed soliton wave (dashed line) over an obstacle of height $W/H = 0.5$, both calculated for Froude number $F = 1.6$.

of the free surface versus Froude number for two values of the relative height $\alpha = W/H$ and three different obstacle shapes. As can be seen from figure 6, increasing the height and width of the obstacle shifts the range $F^* < F < F^{**}$ towards larger values of F^* and F^{**}. Besides, the length of the range F^{**}–F^* is reduced with increase in both the height and the width of the obstacle. The free-surface profiles corresponding to a perturbed soliton wave and a perturbed uniform flow are shown in figure 7.

4.3. *Weir and pouring flows*

In the present formulation of the problem weir and pouring flows are considered as one and the same problem corresponding to subcritical and supercritical flows, respectively.

For subcritical flows, $F < 1$, the height and geometry of the obstacle at the end of the channel uniquely determine the upstream velocity as well as the entire flow (Vanden-Broeck & Keller 1987). For supercritical pouring flows Dias & Tuck (1991) showed that there are two independent parameters, namely the weir geometry and the Froude number. Moreover, for some combinations of the parameters, they found two

https://doi.org/10.1017/jfm.2011.123 Published online by Cambridge University Press

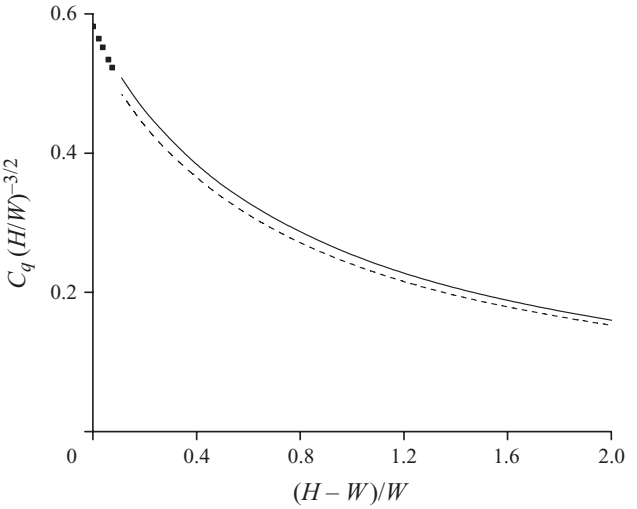


FIGURE 8. The discharge coefficient multiplied by $(H/W)^{-3/2}$ versus $(H-W)/W$ for the channel end shaped as shown in figure 9(*a*, *c*) (solid line) and figure 9(*b*, *d*) (dashed line); solid squares correspond to the thin rectangular weirs taken from Dias & Vanden-Broeck (1989).

families of solutions. For pouring flows, the family of solutions corresponding to a perturbed uniform flow in the case of open channel flows discussed above is referred to as waterfall flows. We will use both these terms depending on the problem under consideration. The other type of solution is called the soliton type as in the case of open channel flows.

For weir flows $F \to 0$, so they are substantially subcritical, and thus the flux or discharge Q is determined by the height of the free surface $H - W$ and the cross-sectional area $\alpha = (H - W)B$ above the weir of width B:

$$Q = C_q \sqrt{g(H-W)}\alpha. \tag{4.4}$$

By taking into account the fact that the flux in the channel flow $Q = UHB$ and the Froude number $F = U/\sqrt{gH}$, the discharge coefficient C_q in the case of two-dimensional flows can be expressed as follows (Vanden-Broeck & Keller 1987):

$$C_q = F\left(\frac{H-W}{H}\right)^{-3/2} = F\left(\frac{H-W}{W}\right)^{-3/2}\left(\frac{W}{H}\right)^{-3/2}. \tag{4.5}$$

In practice (Ackers *et al.* 1978), for a small ratio $(H - W)/W$, or $H/W \approx 1$, the discharge coefficient is considered as a function of the dimensionless ratio $(H - W)/W$ and other dimensionless geometrical parameters.

Figure 8 shows the discharge coefficient multiplied by $(H/W)^{-3/2}$ as a function of the ratio $(H - W)/W$ for the weir shaped as shown in figures 9(*a*) and 9(*c*) (solid line) and for that shaped as shown in figures 9(*b*) and 9(*d*) (dashed line). The results of Vanden-Broeck & Keller (1987) for thin rectangular weirs are also shown by solid squares. The difference between the solid and dashed lines is quite small. It means that the shape of the weir affects the discharge coefficient only slightly. Due to this fact our results for the weir without a rounded spillway agree with the results obtained by Vanden-Broeck & Keller (1987) for thin rectangular weirs. Over the entire range of $(H - W)/W$ in figure 8, the flow remains subcritical.

https://doi.org/10.1017/jfm.2011.123 Published online by Cambridge University Press

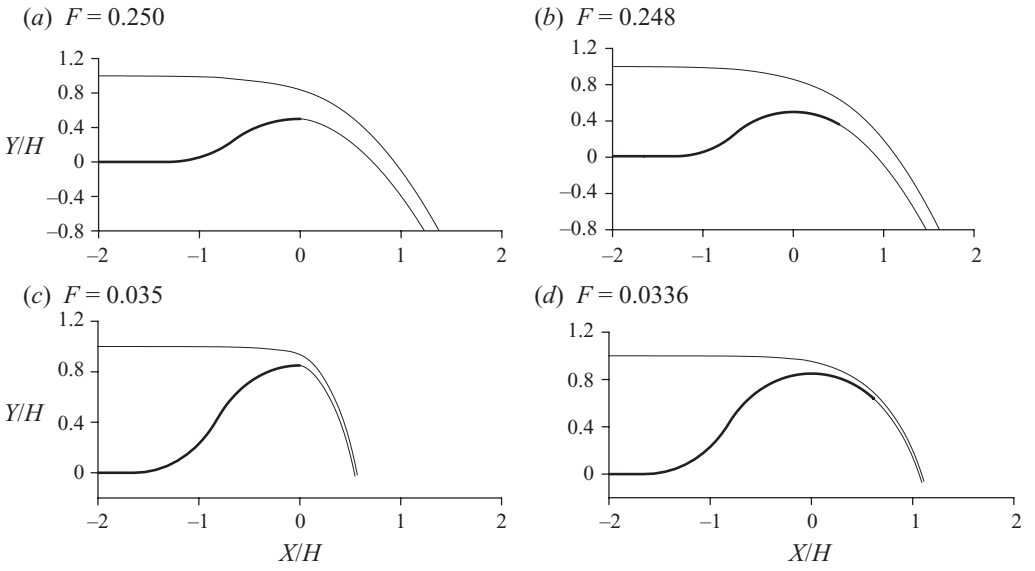


FIGURE 9. Free-surface profiles of sheet subcritical flows with a fixed point of flow separation (*a*) and (*c*) and smooth flow detachment from the cylindrical spout (*b*) and (*d*). The height of the obstacle $W/H = 0.5$ for (*a*) and (*b*) and $W/H = 0.85$ for (*c*) and (*d*).

Figure 9 shows the free-surface profiles for subcritical flows over a bottom surface consisting of two circular arcs of radius $R = H$. The length of each circular arc for cases (*a*) and (*c*) is the same and equal to $S_1 = R\delta_1$, where $\delta_1 = \cos^{-1}[W/(2R)]$. For cases (*b*) and (*d*) the length of the second circular arc, from which the flow separates, is equal to $S_2 = R\delta_2$, where $\delta_2 = \delta_1 + \delta$ and δ is the angle of flow separation from the cylindrical spout. In figures 9(*b*) and 9(*d*) only the wetted part of the cylindrical spout is shown. For cases (*a*) and (*c*) the curvature of the free surface at the point of flow detachment is infinite, while for the smooth separation it is equal to the spout curvature $1/R$.

For subcritical flows the free surface becomes flat at a finite distance from the trailing edge. Otherwise a wave perturbation propagating upstream or downstream would be excited.

For supercritical flows, two types of inflow perturbations can be distinguished. The first is caused by the end of the channel, and it is similar to that occurring for subcritical flows. The second type may occur only for supercritical flows if the gradient of the free surface tends to zero at infinity. Clearly velocity perturbations decay no faster than the gradient of the free surface tends to zero. This type of perturbation may occur because perturbations on the free surface cannot propagate upstream. For the case of open channel flows considered in § 4.2, in addition to the perturbed uniform inflow solution, Vanden-Broeck (1987) found a second type of solution associated with a soliton wave, whose wavelength is infinite. The last means that at a finite distance from the crest of the wave the free surface is not parallel to the x-axis and the velocity magnitude is somewhat different from the inflow velocity U at infinity. The same type of solution for flows over weirs was found by Dias & Tuck (1991) in addition to the waterfall solution. Note that both the waterfall- and the soliton-type solutions are uniform at infinity. However, the numerical results

https://doi.org/10.1017/jfm.2011.123 Published online by Cambridge University Press

	$F=1$			$F=2$			$F=5$		
$-\varphi^*/q$	x^*/h	ε_1	W^*/H	x^*/h	ε_1	W^*/H	x^*/h	ε_1	W^*/H
-5	4.25	7.4×10^{-3}	0.1378	4.83	2.4×10^{-4}	0.05454	4.95	4.2×10^{-4}	0.007785
-10	9.11	8.4×10^{-4}	0.1378	9.79	2.3×10^{-7}	0.05453	9.91	1.8×10^{-8}	0.007784
-15	14.05	4.2×10^{-4}	0.1378	14.76	2.4×10^{-10}	0.05467	14.88	9.8×10^{-12}	–

TABLE 2. Effect of the truncation of the flow region upstream on the error in (3.14) for the waterfall solution at zero height of the trailing edge and the height of the trailing edge for which the free surface becomes flat at a finite distance upstream for three values of the Froude number.

discussed below show that the soliton-type solution has a larger wave elevation than the waterfall-type one and requires a longer computational region.

Both the waterfall- and the soliton-type solutions are a two-parameter family of solutions, the parameters being the height of the weir and the Froude number. If we apply the additional condition (3.14) providing the fastest decay rate of velocity perturbations upstream (or a flat free surface at a finite distance from the end of the channel), then this condition selects a unique solution out of the family of waterfall solutions. It should be noted that the flow is uniform at infinity for all types of solutions. However, for the selected unique solution the decay rate is so fast that the solution can be considered as 'uniform at a finite distance' in a computational sense.

The present formulation of the problem naturally corresponds to the particular solution with a flat free surface at a finite distance upstream because the slope of the free surface $\beta_2=0$ in the region truncated upstream, $\varphi<-\varphi^*$. For other solutions some error ε_1 caused by the truncation occurs in (3.14). However, this error tends to zero as $\varphi^*\to\infty$. This can be seen from table 2 where the results for both types of solution are presented. The column ε_1 shows the magnitude of the left-hand side of (3.14) for height $W/H=0$ and various values of φ^*, which determine the length of the flow region x^* upstream taken in the solution of the system of equations. It can be seen that $\varepsilon_1\to0$ as $\varphi^*\to\infty$ for all Froude numbers presented in the table. The larger the Froude number, the faster the convergence of $\varepsilon_1\to0$. The trailing edge height W^* corresponding to the particular solution with a flat free surface at a finite distance, φ^*, is calculated using (3.14), and it does not depend on the value of φ^*. The last means that the value of φ^* is chosen large enough for the perturbations caused by the end of the channel to be nearly decayed and not to affect the calculated value of the height W^*. On the other hand, φ^* should not be very large so that (3.14) can be solved using standard arithmetic tools . As can be seen from the last column of table 2, the computation of W^* for $F=5$ and $\varphi^*=-15$ requires more figures in the number representation than the standard computer arithmetic offers. On the other hand, smaller values of $|\varphi^*|$ provide a sufficiently accurate computation of the height W^* for $F=5$.

Examples of waterfall- and soliton-type solutions for a channel ending with a sharp vertical trailing edge $W/H=0.36$, which is the maximal possible height W_{max} obtained by the present method, are shown in figure 10. In case (a), the soliton (solid line) and the waterfall (dotted line) solutions are closer to each other. This is due to the fact that these two types of solutions tend to the same limit as the height of the edge increases to its maximal possible value for a given Froude number. For smaller heights the maximal elevation of the free surface for the soliton-type solutions increases, while for the waterfall-type ones it decreases. The computations of Dias

https://doi.org/10.1017/jfm.2011.123 Published online by Cambridge University Press

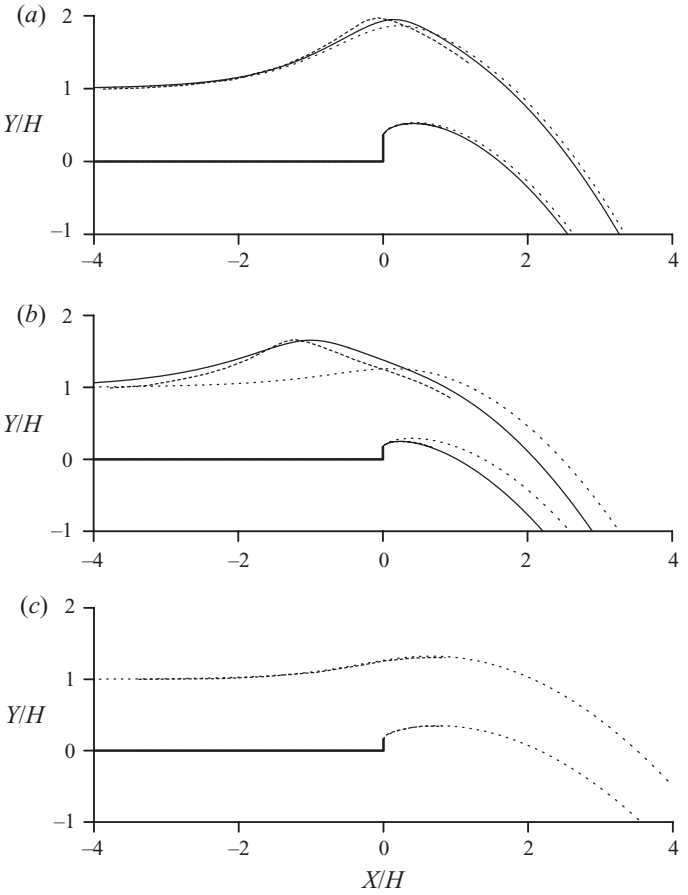


FIGURE 10. Computed waterfall (dotted lines) and soliton (solid lines) types of solutions for $F = 1.46$ and $W/H = 0.36$ (a), $F = 1.27$ and $W/H = 0.17$ (b) and $F = 1.66$ and $W/H = 0.16$ (c) are compared with soliton type solutions of Dias & Tuck (1991) (dashed lines) for cases (a) and (b) and waterfall type solution for case (c); in case (a) $W/H = 0.37$ for the dashed line.

& Tuck (1991) using the series truncation method are shown as a dashed line for the soliton-type solution for $W/H = 0.37$. It can be seen that both predictions are in reasonably good agreement. The difference occurs due to the smaller length of the flow region taken in the calculations with the use of the series truncation method. This length can hardly be increased, which is due to the logarithmic singularity in the solution of the problem. The results for $F = 1.27$ and $W/H = 0.17$ are shown in figure 10(b). The difference between the soliton-type and the waterfall-type solutions is much greater than in the previous case due to the smaller height of the edge. Agreement between the waterfall-type solutions predicted by the present method and the series truncation method for $F = 1.66$ and $W/H = 0.16$ (figure 10c) is quite good because the waterfall-type solution decays much faster upstream than the soliton-type one. The same agreement is expected for the waterfall-type solutions for cases (a) and (b) (not shown).

The solid line in figure 11 shows the trailing edge height W^* for the solution with a flat free surface at a finite distance from the end of the channel. This height is

https://doi.org/10.1017/jfm.2011.123 Published online by Cambridge University Press

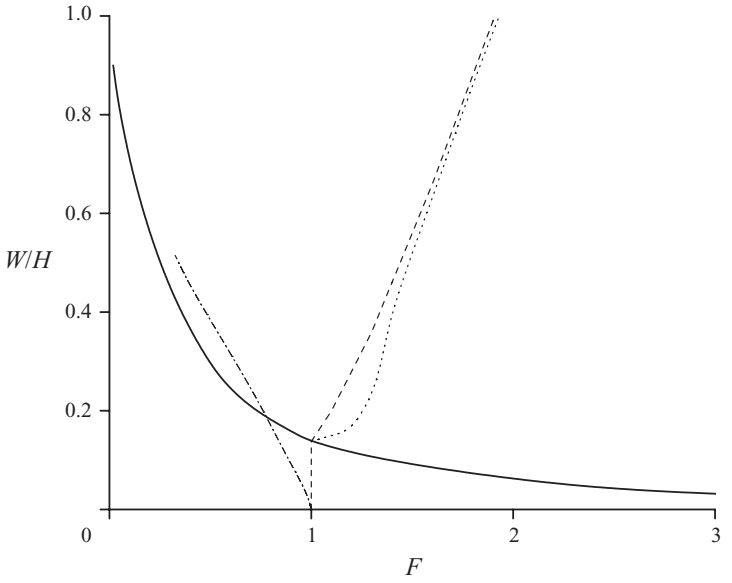


FIGURE 11. Froude number dependence of the height of a trailing edge shaped according to (4.2) corresponding to a flat free surface at a finite distance from the trailing edge (solid line); for $F > 1$ the dashed line is the upper bound of the heights for which both waterfall-type and soliton-type solutions exist; the dotted line corresponds to the lower bound of the heights for which soliton-type solutions exist; the dash-dotted line corresponds to the open-channel flows taken from Dias & Vanden-Broeck (1989).

determined by the Froude number, and it is unique both for subcritical and for supercritical flows. In order to select this type of solutions out of the family of waterfall solutions for the case of supercritical flows, an additional condition, (3.14), has been imposed. The height W^* decreases monotonically with increasing Froude number, and it is continuous in going from subcritical to supercritical flows.

For a uniform inflow at infinity the dashed line in figure 11 shows the maximal possible height of the trailing edge for which a solution can be obtained. For this height the waterfall and the soliton types of solutions coincide. In the region between the dashed and the dotted line both the soliton and the waterfall types of solutions exist, i.e. the dotted line shows the minimal height of the trailing edge for the soliton type of solutions. The minimal height for the waterfall solution is zero.

The dash-dotted line in figure 11 corresponds to the obstacle in a channel of infinite length taken from Dias & Vanden-Broeck (1989). Although the obstacle geometry in the present calculations is quite different from the triangles used in the computations of Dias & Vanden-Broeck (1989) for channel flows, the results both for channel and weir ($F < 1$) flows are rather close to each other for Froude numbers $F < 0.8$. The difference of the results in the range $0.8 < F < 1$ shows the effect of the channel end on the whole of the flow.

Figure 12 shows for $F = 1.1$ the limiting configurations of free-surface profiles corresponding to zero (a) and the maximal (b) height of the rounded trailing edge. Only the wetted part of the edge is shown here. It can be seen that the gradient of the free surface is negative for case (a) and positive for case (b) as the trailing edge is approached. Thus, there exists a trailing edge height such that the free surface far enough upstream becomes parallel to the x-axis. This case shown in figure 12(c)

https://doi.org/10.1017/jfm.2011.123 Published online by Cambridge University Press

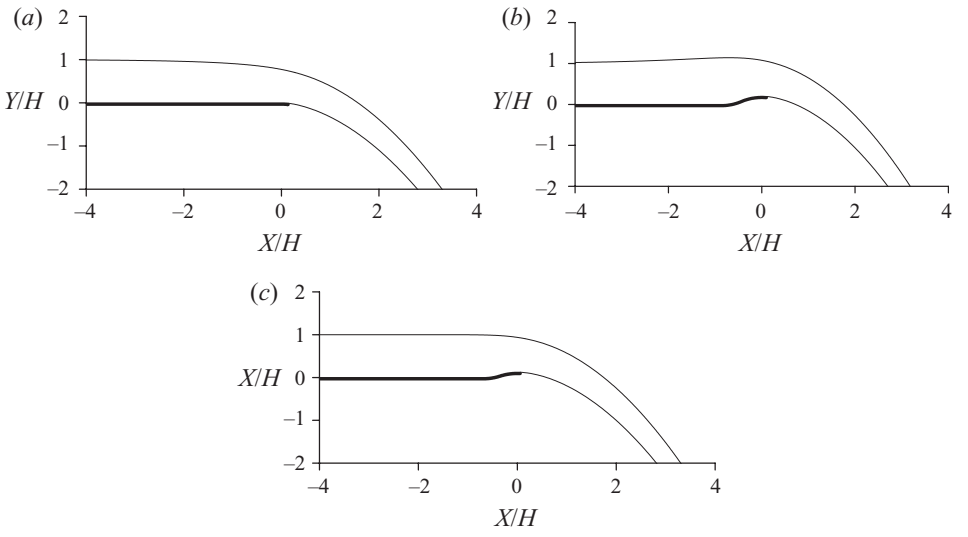


FIGURE 12. Free-surface profiles for Froude number $F = 1.1$ and different heights of a trailing edge of radius $R/H = 1$: zero height (a), the maximal height $W_{max}/H = 0.2$ (b) and the height $W^*/H = 0.125$ (c) for which the free surface becomes flat at a finite distance from the end of the channel.

corresponds to a uniform inflow at finite distance from the end of the channel. It can be seen that the free surface is parallel to the bottom upstream and starts to lower near the trailing edge.

For heights of the trailing edge larger than $W_{max}/H = 0.2$ the iteration process diverges starting with oscillations of the free surface upstream of the trailing edge. This may occur because a supercritical inflow goes into a subcritical flow due to the free-surface rise and the corresponding decrease in the local velocity. Because of this, perturbations caused by the trailing edge can move upstream.

For zero height of the trailing edge at $F = 2$ (figure 13a), the negative gradient of the free surface upstream of the trailing edge is somewhat smaller than in figure 12(a), which is due to a smaller effect of gravity. In the case of the maximal height of the trailing edge (figure 13b), the computed angle of flow separation $\delta = -0.0749$ is negative, so the ordinate of the separation point is less than the maximal height W_{max} of the trailing edge. The y-component of the velocity is positive, thus forming a free falling jet directed upward. The computed velocity magnitude at the top of the jet $v/u = 0.17$, so the free surface almost reaches the maximal value $y_{max}/h = 1 + F^2/2 = 3$.

For heights of the trailing edge larger than $W_{max}/H = 1.09$ the iteration process diverges starting with oscillations of the free surface near the top of the falling jet. The maximal value of the slope of the free surface increases, and the iteration process breaks down. Note that the value $\beta_{2max} \approx 38^\circ$ computed for the falling jet shown in figure 13(b) is larger than 30°, which is the maximal angle of slope for free-surface waves. This may be caused by the flow asymmetry in the present case.

The angle of flow separation normalized by π is shown in figure 14 for the case of a uniform inflow. The geometry of the cylindrical spout is given by (4.2) with $R = H$ and the height W^* as a function of the Froude number shown in figure 11 by the solid line. For $F \to 0$ the angle δ/π tends to the value ≈ 0.23, which is close to the value $\delta/\pi = \cos^{-1}(2/3)/\pi \approx 0.27$ corresponding to the angle of separation of a small solid ball moving along the spout under gravity.

https://doi.org/10.1017/jfm.2011.123 Published online by Cambridge University Press

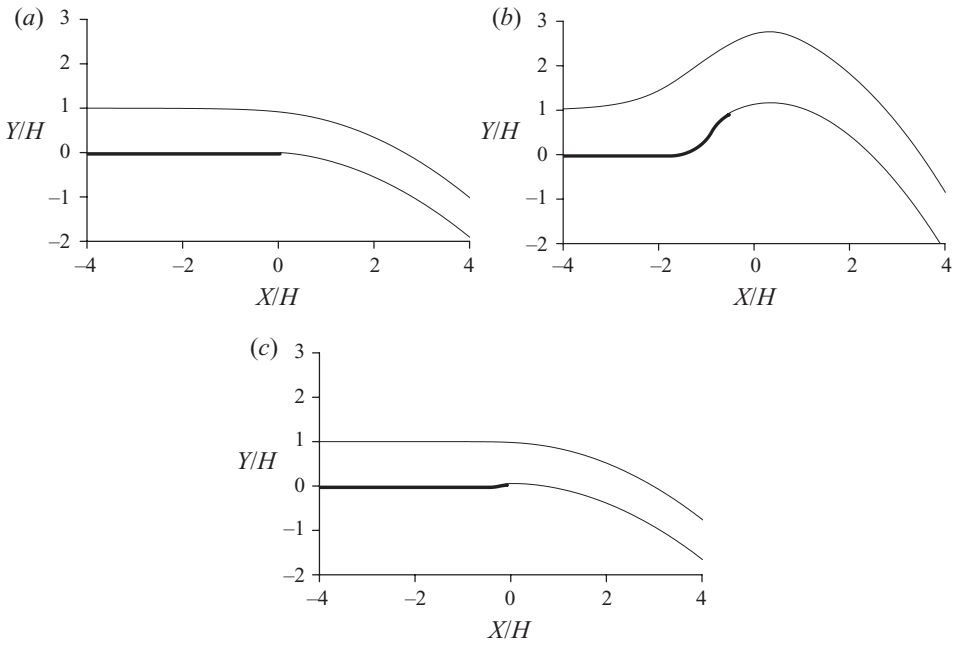


FIGURE 13. Free-surface profiles for Froude number $F = 2$ and different heights of the trailing edge: zero height (a), the maximal height $W_{max}/H = 1.09$ (b) and the height $W^*/H = 0.0545$ (c) for which the free surface becomes flat at a finite distance from the end of the trailing edge.

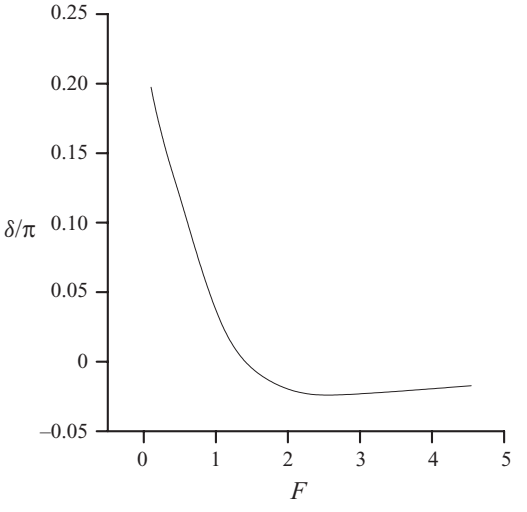


FIGURE 14. The angle of flow separation from the trailing edge in the case of the perturbed uniform flow. The shape of the trailing edge is given by (4.2) and the height is computed as shown in figure 11 by the solid line.

With increasing Froude number the angle of flow separation δ/π decreases and becomes negative for $F > 1.35$. For negative values of δ/π, the flow does not reach the top point of the spout, so the wetted height of the spout is somewhat less than W^*. With a further increase in the Froude number the angle of flow separation $\delta/\pi \to 0$

https://doi.org/10.1017/jfm.2011.123 Published online by Cambridge University Press

since the height W^* and correspondingly the angle $\gamma = \cos^{-1}[1 - W/(2R)]$ in (4.1) also tend to zero.

The present model of flow around a rounded spout, which includes only gravity, does not predict the 'teapot effect'. However, if the point of flow separation is given on the underside of the spout far enough from the rounded part, it is obvious that the geometry of the spout does not affect the channel flow on the underside of the spout. In this case the location of flow separation can be anywhere on the straight underside as shown by Vanden-Broeck & Keller (1989).

5. Conclusions

A complete nonlinear solution of a sheet inviscid flow separating from a rounded trailing edge is presented in the form of a system of integral and integro-differential equations, for the solution of which a numerical method has been developed. The system of equations is derived by using an advanced hodograph method, which enables one to derive analytical expressions for the complex velocity and for the complex potential, both defined in the first quadrant of the parameter plane. The solution obtained provides a general solution for several problems considered in the literature separately, namely open-channel flows with an arbitrarily shaped bottom, weir and pouring flows.

Numerical results are presented for a wide range of Froude numbers including both the subcritical and supercritical flow regimes. Besides, the calculations have been done using the flow potential as an independent variable and asymptotic expressions for the integrals in the expression for the derivative of the mapping function. This made it possible to overcome the difficulty caused by the logarithmic singularity and compute long thin jets in a free fall.

Particular attention is given to pouring flows with separation from a shaped trailing edge. For the subcritical flow regime corresponding to weir flows, a solution of the problem is uniquely determined by the height and geometry of the weir. For supercritical flows two families of solutions are obtained. The first type is the waterfall-type family of solutions predicted by Dias & Tuck (1991) for channels ending with a flat vertical trailing edge. The second family of solutions is similar to the perturbed soliton waves found by Vanden-Broeck (1987) for open channel flows with obstructions. A particular solution has been chosen out of the family of waterfall solutions for which the free surface becomes flat at a finite distance from the trailing edge. This solution is continuous in going from subcritical to supercritical flows.

The Brillouin–Villat criterion is applied to determine the location of the point of flow separation from the rounded trailing edge. The obtained results show that the inclusion of gravity alone does not allow one to predict the 'teapot effect'.

The authors are grateful to the anonymous referees, who suggested several important improvements in the presentation of the results. University of Ulsan and Hyundai Heavy Industries Co. Ltd. are also acknowledged for their support of the present study.

REFERENCES

Ackers, P., White, W. R., Perkins, J. A. & Harrison, A. J. M. 1978 *Weirs and Flumes for Flow Measurements*. Wiley.

Benjamin, T. B. 1966 Internal waves of finite amplitude and permanent form. *J. Fluid Mech.* **25** (2), 241–270.

https://doi.org/10.1017/jfm.2011.123 Published online by Cambridge University Press

Birkhoff, G. & Zarantonello, E. H. 1957 *Jets, Wakes, and Cavities*. Academic.

Brillouin, M. 1911 Les surfaces de glissement de Helmholtz et la resistance des fluids. *Ann. Chim. Phys.* **23**, 145–230.

Chaplygin, S. A. 1910 *About Pressure of a Flat Flow on Obstacles. On the Airplane theory*. Moscow University, 49 p.

Dias, F., Vanden-Broeck, J.-M. & Keller, J. B. 1988 Flows over rectangular wiers. *Phys. Fluids* **31**, 2071–2076.

Dias, F. & Vanden-Broeck, J.-M. 1989 Open channel flows with submerged obstructions. *J. Fluid Mech.* **206**, 155–170.

Dias, F. & Vanden-Broeck, J.-M. 1990 Flows emerging from a nozzle and falling under gravity. *J. Fluid Mech.* **213**, 465–477.

Dias, F. & Tuck, E. O. 1991 Weir flows and waterfalls. *J. Fluid Mech.* **230**, 525–539.

Dias, F. & Vanden-Broeck, J.-M. 2004 Trapped waves between submerged obstacles. *J. Fluid Mech.* **509**, 93–102.

Forbes, L. K. & Schwartz, L. W. 1982 Free-surface flow over a semicircular obstruction. *J. Fluid Mech.* **114**, 299–314.

Gurevich, M. I. 1965 *Theory of Jets in Ideal Fluids*. Academic.

Joukovskii, N. E. 1890 Modification of Kirchoff's method for determination of a fluid motion in two directions at a fixed velocity given on the unknown streamline. *Math. Coll.* **15**, 121–278.

Keller, J. B. 1957 Teapot effect. *J. Appl. Phys.* **28**, 859–864.

Reiner, M. 1956 The teapot effect. *Phys. Today* **9** (9), 16.

Semenov, Y. A. 2003 Complex potential of unsteady free-boundary flow. *Vestnik Khersonskogo Universiteta* (in Russian), **2**, 384–387.

Semenov, Y. A. & Yoon, B.-S. 2009 Onset of flow separation at oblique water impact of a wedge. *Phys. Fluids* **21**, 112103–112111.

Vanden-Broeck, J.-M. 1987 Free-surface flow over an obstruction in a channel. *Phys. Fluids* **30**, 2315–2317.

Vanden-Broeck, J.-M. & Keller, J. B. 1986 Pouring flows. *Phys. Fluids* **29** (12), 3958–3961.

Vanden-Broeck, J.-M. & Keller, J. B. 1987 Weir flows. *J. Fluid Mech.* **176**, 283–293.

Vanden-Broeck, J.-M. & Keller, J. B. 1989 Pouring flows with separation. *Phys. Fluids* A **1**, 156–158.

Villat, H. 1914 Sur la validite des solutions de certains problemes d'hydrodynamique. *J. Math. Pure Appl.* **20**, 231–290.

https://doi.org/10.1017/jfm.2011.123 Published online by Cambridge University Press